

Article

Development of a Hybrid Fixed-Wing UAV Aeromagnetic Survey System and an Application Study in Chating Deposit

Ning Lu ^{1,2,3} , Yongzai Xi ^{1,2,3} , Hongshan Zheng ^{1,2,3}, Weidong Gao ^{1,2,3}, Yongbo Li ^{1,2,3} , Yu Liu ^{1,2,3}, Zhiqiang Cui ^{1,2,3}, Guixiang Liao ^{1,2,3} and Junjie Liu ^{1,2,3,*}

- ¹ Institute of Geophysical and Geochemical Exploration, Chinese Academy of Geological Sciences, China Geological Survey, Langfang 065000, China; luning@mail.cgs.gov.cn (N.L.); xyongzai@mail.cgs.gov.cn (Y.X.); zhongshan@mail.cgs.gov.cn (H.Z.); gweidong@mail.cgs.gov.cn (W.G.); lyongbo@mail.cgs.gov.cn (Y.L.); yuliu@mail.cgs.gov.cn (Y.L.); czhiqiang@mail.cgs.gov.cn (Z.C.); lguixiang@mail.cgs.gov.cn (G.L.)
- ² Key Laboratory of Geophysical Electromagnetic Probing Technologies, Ministry of Natural Resources, Langfang 065000, China
- ³ National Research Centre of Modern Geological Exploration Engineering Technology, Langfang 065000, China
- * Correspondence: ljunjie@mail.cgs.gov.cn

Abstract: In recent years, the development of airborne magnetic survey technology based on unmanned aerial vehicles (UAVs) has been rapidly advancing. The commonly used systems are the fixed-wing UAV-based, multi-rotors UAV-based, and unmanned helicopters-based magnetic survey systems. And, a type of hybrid UAV that uses a vertical takeoff and landing (VTOL) and fixed-wing cruise mode is increasingly being used to carry airborne magnetic survey systems. To meet the requirements of most UAVs for small-sized and lightweight payloads, a miniature magnetic survey system was developed and integrated into a hybrid fixed-wing UAV and formed an aeromagnetic survey system. And, a peripheral mineral exploration test was conducted in a known porphyry copper–gold deposit in southeastern China using the system. By processing the collected magnetic data with 3D inversion of susceptibilities, potential ore-bearing intrusive rocks were quickly identified and delineated, providing clues for peripheral mineral exploration in the mining area.



Citation: Lu, N.; Xi, Y.; Zheng, H.; Gao, W.; Li, Y.; Liu, Y.; Cui, Z.; Liao, G.; Liu, J. Development of a Hybrid Fixed-Wing UAV Aeromagnetic Survey System and an Application Study in Chating Deposit. *Minerals* **2023**, *13*, 1094. <https://doi.org/10.3390/min13081094>

Academic Editor: Amin Beiranvand Pour

Received: 25 June 2023

Revised: 6 August 2023

Accepted: 15 August 2023

Published: 16 August 2023



Copyright: © 2023 by the authors. Licensee MDPI, Basel, Switzerland. This article is an open access article distributed under the terms and conditions of the Creative Commons Attribution (CC BY) license (<https://creativecommons.org/licenses/by/4.0/>).

Keywords: unmanned aerial vehicle; UAV; hybrid fixed-wing UAVs; vertical taking off and landing; VTOL; aeromagnetic; mineral prospecting; Chating deposit

1. Introduction

Aeromagnetic surveying has always been an important foundational technique in mineral exploration. The manned fixed-wing and helicopter-borne aeromagnetic surveys have achieved countless remarkable results worldwide. The UAV-borne aeromagnetic survey is an airborne geophysical survey method that utilizes UAV platforms. In recent years, the increasing use of UAVs in various fields has led to the emergence of UAV-based geophysical surveys known as a hot research area [1–17]. The common types of UAVs presently used for an aeromagnetic survey are fixed-wing UAVs, unmanned helicopters (UHs), and multi-rotor UAVs [18]. Among these types of UAV aeromagnetic survey systems, fixed-wing UAVs and multi-rotor UAVs are commonly used and both have found their respective fields of expertise in terms of application. Fixed-wing UAVs have the advantages of long endurance and high speed, making them suitable for rapid measurements of large areas. However, they require runways for take-off and landing and are not suitable for low-speed and high-resolution surveys. Multi-rotor UAVs can perform tasks automatically and are easy to operate with terrain following function making them suitable for small-scale, high-resolution surveys. They are relatively cheap but have poor payload capability and short flight duration, compared to medium- and large-sized fixed-wing UAVs. Unmanned helicopters can take-off and land vertically and are suitable for

missions in complex terrain or dangerous areas, such as volcanoes. They can change flight speed according to mission needs, but their complex mechanical structure brings higher operational risks and maintenance costs in case of failures in complex survey conditions.

The Institute of Geophysical and Geochemical Exploration (IGGE) has been continuously focusing on, investigating, and implementing UAV geophysical surveys since the 2010s and has made great progress in this area [19]. We developed the first functional fixed-wing UAV airborne geophysical survey system in China using the CH3 UAV, and we have conducted a total of 150,000 km of field surveying [20]. In addition to fixed-wing drones, we have also carried out research and applications of UH and multi-rotor drones in geophysical surveys [21,22]. During the process of all the work above, the need for UAVs with VTOL capabilities and fast flight speed has become increasingly evident. Then, we discovered that this type of hybrid fixed-wing UAV was able to meet our requirements. This type of UAV achieves VTOL in multi-rotor mode and cruises in fixed-wing mode. It has the advantages of both multi-rotor UAVs' ability to take off and land vertically and fixed-wing UAVs' high-speed flight, long endurance, and large payload capability. It is very suitable as an aeromagnetic survey platform.

We have developed a hybrid fixed-wing UAV-borne aeromagnetic survey system and successfully completed an experimental measurement around a known copper–gold deposit in southern China in 2021. The measurement results provided intuitive and effective clues for prospecting work around the mining area, which shows that the systems have essentially reached production capacity.

2. Development of the Hybrid Fixed-Wing UAV Aeromagnetic Survey System

The hybrid fixed-wing UAV aeromagnetic survey system developed by IGGE, Langfang, China (iHFUAM) was designed to satisfy unique requirements for UAV aeromagnetic surveys. The system was designed to enable rapid deployment with vertical takeoff and landing capabilities, while also achieving high flight speeds to efficiently cover large areas. The iHFUAM comprises a self-developed miniaturized aeromagnetic system and a JOUAV-manufactured CW-30 Hybrid fixed-wing UAV.

2.1. Miniaturized Aeromagnetic Instruments Suitable for Drones

In general, except for some large or specially designed ones, the payload and capacity of conventional UAVs are significantly lower than those of manned aircraft, making it impractical to directly integrate traditional aeromagnetic instruments designed for manned aircraft onto UAV platforms. Therefore, there is a need to develop smaller and lighter aeromagnetic instruments specifically for use on UAV platforms. While there are several established aeromagnetometers for UAVs, they are often expensive or time-consuming to acquire, leading us to develop our own instruments.

To address the need for small and lightweight aeromagnetometers for UAVs, we developed the Miniature Aerial Magnetic System of IGGE (iMAMS) with support from the National Key Research and Development Program. The iMAMS is a self-designed system that includes the following main components: Front-end Analog Component, Signal Transformation Component, Synchronization and Trigger Component for Global Navigation Satellite System (GNSS), Master Card, and Power Component.

With dimensions of 150 mm × 150 mm × 130 mm, a weight of approximately 2.5 kg individually, and about 6 kg in a measuring set, the iMAMS is significantly smaller and lighter than those typical aeromagnetic systems for manned aircrafts. The iMAMS enables simultaneous acquisition of GNSS, altimeters, fluxgate, and four channels of optically pumped magnetometer (OPM) data. It also provides VGA/HDMI for video output, USB and serial ports for system control, and interfaces for communication with UAVs and remote link access specially designed to meet the requirements for UAV measurements. Figure 1 shows the main components of the iMAMS that only use fluxgate sensors for measurements. When higher precision measurements are required, OPM can be additionally connected with the fluxgate used as flight maneuvers data. When using only fluxgate magnetometers

for measurement, the system weight can be reduced by about 1 kg to approximately 5 kg. In order to be compatible with more usage scenarios, the host is equipped with 19 interfaces, most of which are actually redundant. If only fluxgate sensors are used for measurement, the recording equipment would not require so many interfaces, and the volume and weight would naturally be reduced. It is entirely possible to develop a dedicated fluxgate measurement system with a weight of 2–3 kg by completely removing unnecessary components.



Figure 1. A typical set of components of iMAMS.

The main parameters of the data acquisition system (DAS) of the iMAMS are as follows: System noise is 0.1 pT; resolution is 0.35 pT; sampling rate is 800 Hz; measurement frequency is 1 Hz, 5 Hz, 10 Hz, 20 Hz, and 40 Hz optional; and temperature stability is $\pm 5\text{ppb}@100\text{MHz}$. The main parameters of the fluxgate sensor are as follows: The measurement range is $\pm 100\ \mu\text{T}$; the bandwidth is DC~1 kHz; the linearity is $\leq 0.01\%$ of full scale; the time-domain noise is 0.1 nT RMS @10Hz; and the frequency-domain noise is 10~20 pT/ $\sqrt{\text{Hz}}$ @1Hz. The direction error and sensitivity depend on the magnetometer used. Taking the SCINTREX CS-3 magnetometer as an example, the sensitivity is 0.6 pT/ $\sqrt{\text{Hz}}$, and the directional error is $\pm 0.2\ \text{nT}$.

2.2. Integration

2.2.1. Magnetic Interference Background Testing of the UAV

The iHFUAM is based on the CW30 hybrid fixed-wing UAV, which boasts a wingspan of 4 m, a length of 2.1 m, a maximum payload of 6.5 kg, an endurance of 3–6 h, a cruising speed of around 90 km/h, a maximum take-off altitude of 3800 m, and a maximum wind resistance of 12 m/s. CW30 is a hybrid power UAV that utilizes a combination of electric power from batteries for VTOL and switches to a gasoline engine for propulsion during cruising. It possesses the capability for beyond-visual-range communication and flight, subject to obtaining the necessary authorization for such operations.

To reduce the magnetic interference from UAV components (such as engines) on the sensor, we conducted a magnetic interference test on the CW30. We designed a simple grid with a spacing of 0.5 m and an area of 5 m by 4.5 m centered on the cabin and first measured the magnetic field background at the test points. We then separately measured

the magnetic field at each cross point with the propulsion engine off and on. The test, when the propulsion engine was on, has been conducted under simulated airborne thrust power. A CW30 is a relatively small aircraft whose thrust power is not very large; thus, two manufacturer engineers can control the aircraft in front of the wings. The motion test of the wing and tail rudder servos was carried out during the aircraft background test before the engine was started. There was obvious interference when close to the servo, and the servo motors are locked during flight; therefore, the interference of servo movements was not conducted. The measurement results showed that the propulsion engine generated the highest magnetic field, reaching about 150 nT when off and 210 nT when on (Figure 2). These results are similar to those of fixed-wing UAVs with comparable shapes [23]. The maximum magnetic interference from the UAV occurs at the engine and decreases rapidly as the distance from it increases. Therefore, to minimize the impact of propulsion engines, magnetometer sensors should be installed as far away from the engines as possible. In this case, we placed the magnetic sensor 2.5 m away from the propulsion engine to reduce the magnetic interference.

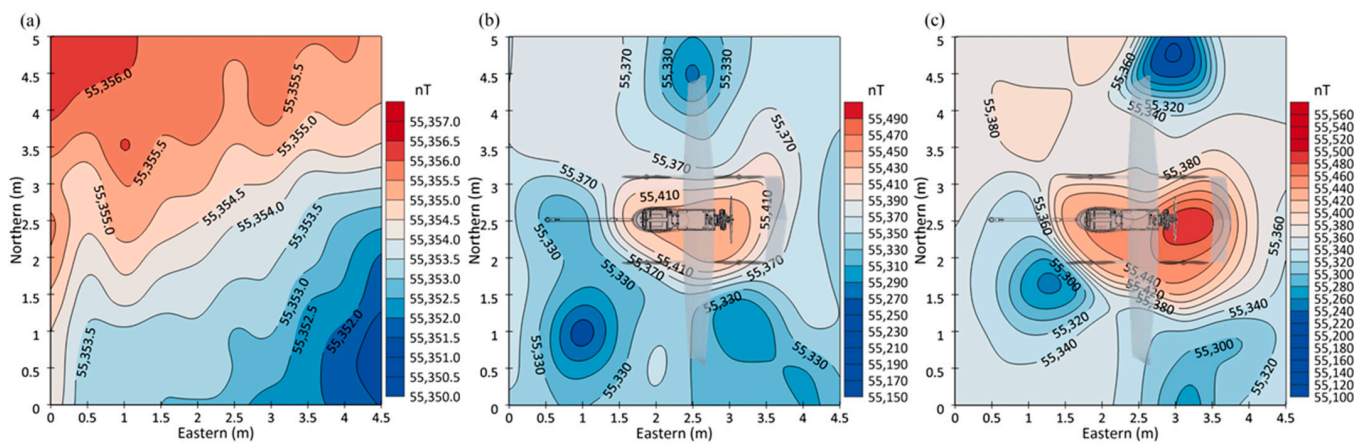


Figure 2. Magnetic interference test of the UAV: (a) Magnetic background of the test area; (b) magnetic field when the power engine is off; (c) magnetic field when the power engine is on.

The way of VTOL in this type of UAV makes it feasible to use a scheme where the aeromagnetometer is suspended a few meters below the UAV. However, the suspended aeromagnetometer may more or less increase the operational difficulty and risk of take-off and landing. Therefore, after comprehensive analyzing, we chose the current type for refitting.

2.2.2. Refitting and Integration

Based on the results of the magnetic background test, we have mounted a CS-VL Cesium magnetometer from SCINTREX on a flexible rigid rod that extends approximately 1.5 m forward from the nose. The rod is fixed to the cabin at one end, with a sensor attached to a specialized engineering plastic bracket located at the other end. The fluxgate is positioned in the middle of the rod. The iMAMS is situated on a specially designed bracket inside the cabin, while the GNSS antenna is secured to the cabin cover and the altimeter is installed beneath the belly. The iHFUAM has a mission payload of approximately 6 kg and is powered by a separate high-density battery pack, enabling the aeromagnetic instruments to function independently of the UAVs' energy source. This allows for simple and efficient flight surveys, with the ability to take off and land on any small, stable, flat surface, such as roads, grassland, and even a vehicle roof (Figure 3).

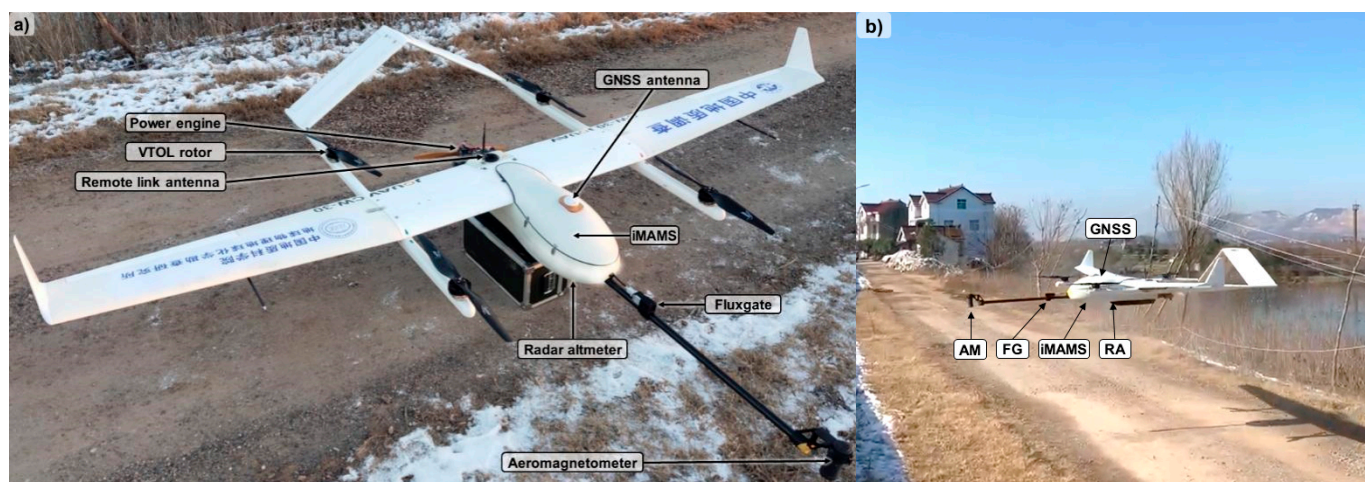


Figure 3. The refitted iHFUAM: (a) Configuration of the system; (b) the status of iHFUAM while taking off from a country road. Abbreviations: AM—aeromagnetometer; RA—radar altimeter; FG—fluxgate.

3. Application in Mineral Prospecting

We conducted an experimental measurement using iHFUAM around the newly discovered Chating copper–gold deposit in Anhui Province, China, with the aim of revealing the magnetic characteristics of the deposit and identifying potential mineralized zones near Chating based on aeromagnetic data. Additionally, we sought to verify the measurement production performance of iHFUAM.

3.1. Geology of the Survey Area

The survey area is situated in the Nanling-Xuancheng ore region (NXOR) of the Middle-Lower Yangtze River Metallogenic Belt (MLYMB). The MLYMB is located along the northern margin of the Yangtze Plate, northwest of which is the Dabie Orogenic Belt. The northern margin of the Yangtze Plate can be further divided into the Northern Sub-Yangtze Foreland Belt in the north and the Jiangnan Uplift Belt in the south, separated by the Chongyang–Changzhou Fault (CCF). The Jiangnan Uplift Belt is part of the Jiangnan Orogenic Belt. Therefore, the Northern Sub-Yangtze Foreland Belt is sandwiched between the Dabie Orogenic Belt and the Jiangnan Orogenic Belt. The MLYMB is an important polymetallic metallogenic belt producing copper, iron, gold, and silver in China. It hosts over 100 types of mineral deposits with proven resources. Over 2200 deposits of nonferrous metals, ferrous metals, precious metals, and rare metals have been found, forming seven mineral concentration areas centered by large- and medium-sized ore clusters, such as Ningwu, Luzong, Tongling, etc. [24–26] (Figure 4a).

In recent years, a cluster of copper–gold–lead–zinc–molybdenum–tungsten polymetallic deposits, such as Chating Cu–Au deposit, Tongshan-Qiaomaishan Cu–W, Magushan Cu–Mo deposit, and Shizishan Cu deposit, have been discovered in NXOR, which has been designated as the eighth metallogenic cluster zone of MLYMB [25]. The NXOR is located along the southeastern margin of the Middle and Lower Yangtze River depression. Most of the area is covered by thick Quaternary overburden. The main structures of the NXOR trend to the NNE, including the Jiangnan Fault (JNF), Kunshan Fault (KSF), Sanli-Hexi Fault (SHF), and Qingshui-Hewan Fault (QHF). At the secondary structural level, the main structures are the east–west-trending Zhouwang Fault (ZWF) and the northwest-trending Ma’anshan-Langxi Fault (MLF). The main fold in the area is the Jingtingshan-Liqiao anticline between LQF and KSF. On both sides of the anticline are two sedimentary basins: Xuancheng Basin in the east and Nanling Basin in the west (Figure 4b).

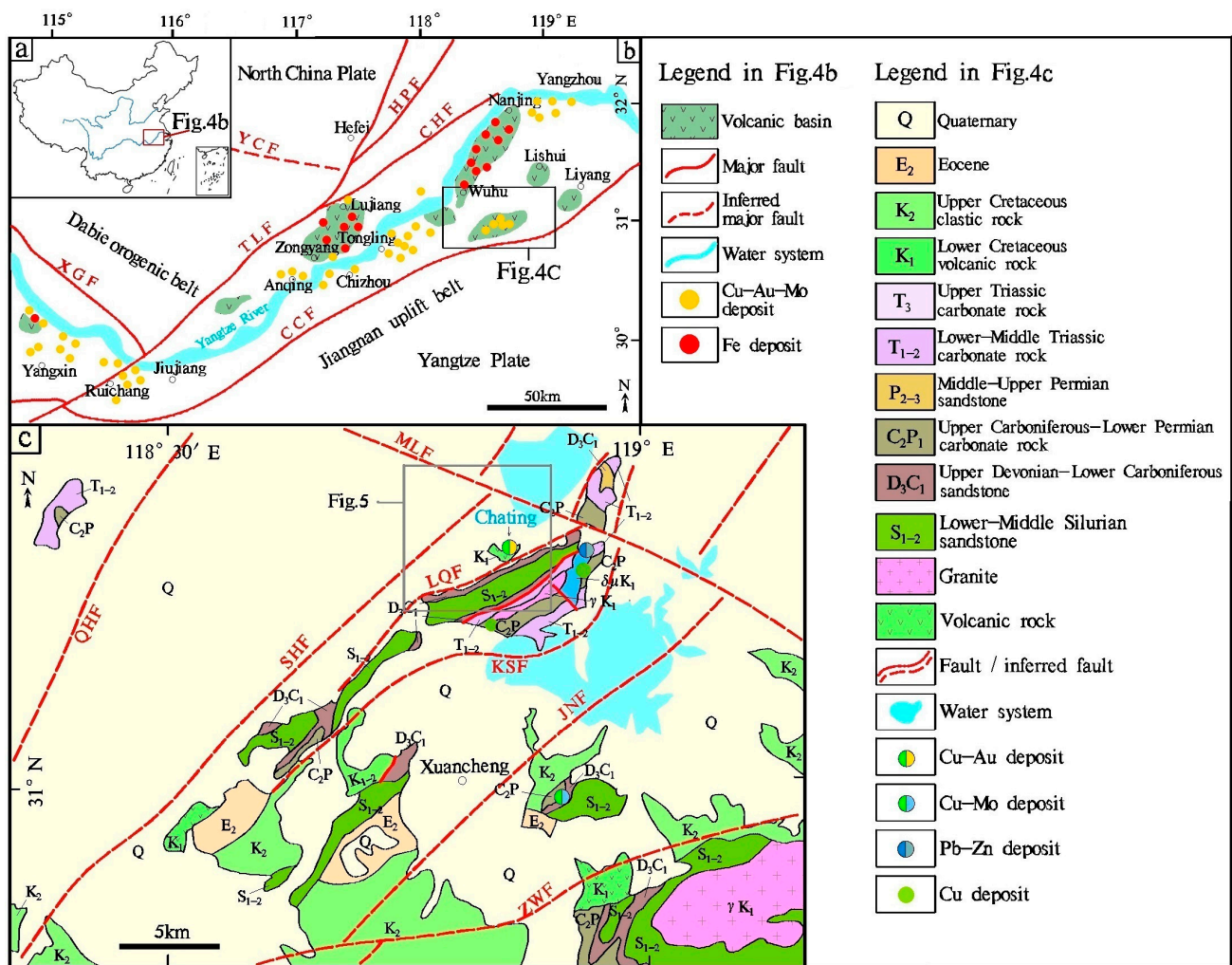


Figure 4. Regional geological map of survey area (modified after [26]): (a) Location of the study area; (b) Sketch of a regional geological map of MLYMB; (c) geological and mineral map of the Xuancheng area. Abbreviations: XGF, Xiangfan-Guangji fault; TLF, Tancheng-Lujiang fault; HPPF, Huanglishu-Poliangting fault; CCF, Chongyang-Changzhou fault; QHF, Qingshui-Hewan fault; SHF, Sanli-Hexi fault; LQF, Liqiao fault; KSF, Kunshan fault; JNF, Jiangan fault; ZWF, Zhouwang fault; MLF, Ma’anshan-Langxi fault.

The Chating deposit is located on the northwest side of the Liqiao anticline. The survey area is mostly underlain by Quaternary sediments, with a thickness of about 20 m that increases from southeast (SE) to northwest (NW). Volcanic rocks of the Upper Cretaceous are exposed south of the mining area. The Liqiao anticline to the southeast is composed of Silurian sandstone, Devonian mudstone, and mainly carbonate rocks of the Permian and Early Triassic. The main tectonic structures in the area are the northeast (NE) and southwest (SW) fractures, with the NE ones being dominant (Figure 5a).

Beneath the Quaternary cover in the Chating ore district are intermediate-acidic terrestrial volcanic rocks of the Lower Cretaceous and terrestrial clastic sedimentary rocks of the Upper Cretaceous. No obvious alteration and mineralization are observed, but strong weathering exists. According to drill core exposures, the quartz diorite porphyry body outlined is nearly vertical and roughly forms a northeast-trending lenticular shape in plain view, over 5 km long and less than 1 km wide at its widest point. Veins of diorite porphyry and quartz diorite porphyry commonly cut the quartz diorite porphyry body. Drill core exposures show that the wall rock of the quartz diorite porphyry body is Lower Triassic limestone. At the contact between the quartz diorite porphyry body and the wall

rock, dolomite and dolomitized limestone are developed, in which no mineralization is observed. The orebody is hosted in a concealed quartz diorite porphyry intrusion with a cover thickness of 100 to 200 m. In plain view, the orebody covers an area slightly larger than 1000 m by 500 m. Drill exploration depth is controlled within 2000 m. Aphanitic agglomerate is developed within the quartz diorite porphyry intrusion. The distribution range of the aphanitic agglomerate is basically consistent with but slightly smaller than the mineralization range, which shows an inverted bell shape. The deep mineralization has not been fully delimited (Figure 5b).

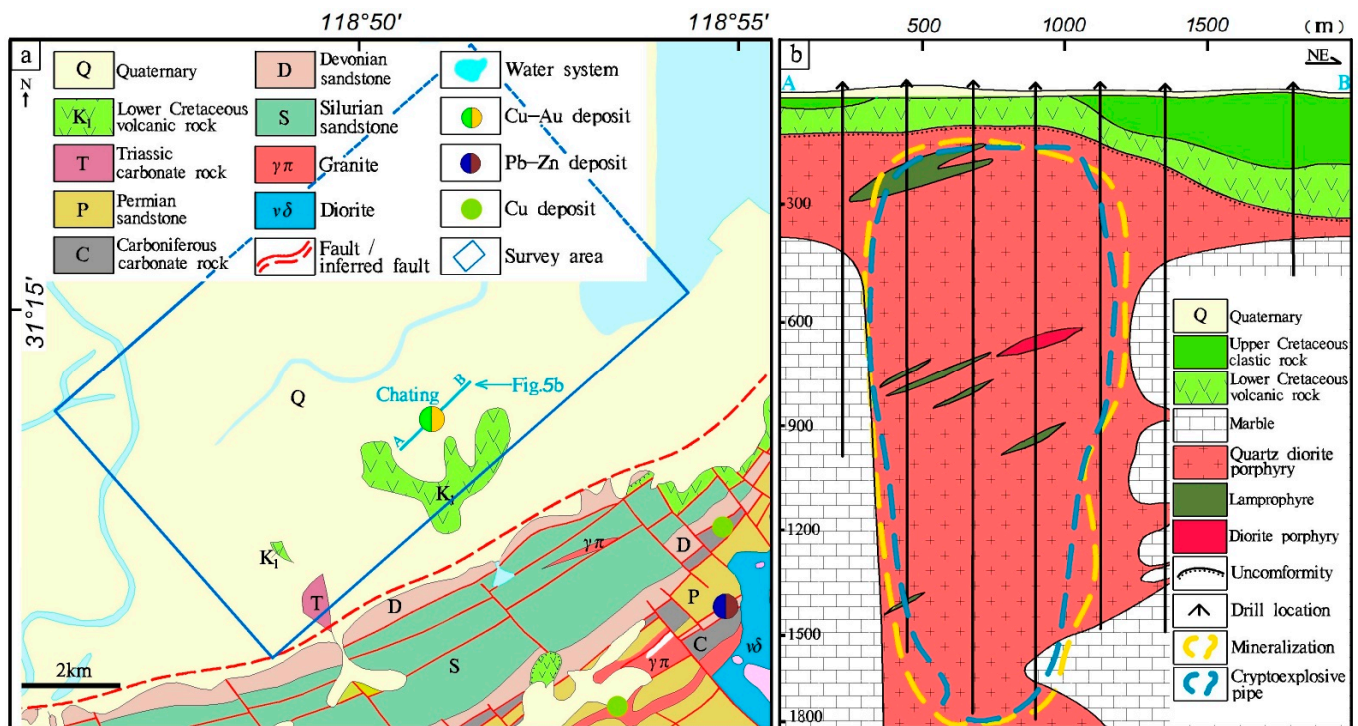


Figure 5. Simplified geological map of Chating area and geological section A–B of Chating deposit (modified after [26]): (a) Geological map; (b) section A–B.

3.2. Magnetic Characteristics of the Chating Ore Area

The magnetic parameters of geological strata, igneous rocks, and ores in the Chating area were statistically obtained using magnetic susceptibility data from rock samples and drill cores. The results are shown in Table 1.

Statistically, in the Chating mining area, Upper Cretaceous agglomerate and clastic rocks have medium to low magnetism, except when a small amount of andesite is developed. Most of the Lower Cretaceous volcanic rocks have medium to low magnetism. The strata of Triassic, Permian, Carboniferous, Devonian, and Silurian have no magnetism or weak magnetism. Granite porphyry has medium to low magnetism. Quartz diorite porphyry, Lamprophyre, and Diorite porphyry have medium to high magnetism. Chalcopyrite ore and copper-mineralized rocks have medium to low magnetism, which is insufficient to directly produce a significant magnetic anomaly different from other magnetic geological bodies.

Overall, the susceptibility of the sedimentary strata in the study area varies within a relatively small range, approximately from 0 to 80×10^{-6} SI. The main intrusive rocks in the area show a significant increase in susceptibility, ranging from approximately 1600 to 3300×10^{-6} SI. Because ore deposits are mostly formed within these strongly magnetic intrusive rocks, defining these rocks with airborne magnetic data can provide very useful exploration insights.

Table 1. Statistical magnetic parameters in Chating area.

Strata and Rock Type	Samples	Susceptibility (10^{-6} SI)		
		Minimum	Maximum	Average
Upper Cretaceous clastic rocks	3	1.36	1.39	1.36
Lower Cretaceous volcanic rocks	120	2.6	3533.1	335.6
Triassic carbonate rocks	60	0.9	23.1	7.9
Permian sandstone	60	0	18	2.5
Carboniferous carbonate rocks	90	0	24.4	2.9
Devonian sandstone	40	0	1195.6	84.8
Silurian sandstone	60	3.1	1470	88.2
Quartz diorite porphyry	270	1.9	6691.9	1673.6
Lamprophyre	180	1.5	7827.7	2654.8
Diorite porphyry	30	110.5	6041.5	3385.5
Copper-bearing breccia	60	1.1	8422.4	486.3
Chalcopyrite ore	60	26.4	2410.9	252.8

3.3. Field Survey

The survey area is mainly agricultural, with a flat terrain and no significant magnetic disturbances, except for some small villages and a town to the west. This makes it suitable for UAV-borne aeromagnetic surveys (Figure 6a). We designed 47 survey lines in the SE-NW direction, perpendicular to the main structural orientation, with a total length of about 350 km. The iHFUAM is very portable and only needs two pilots and a geophysicist to conduct the flight surveys. In this trial, we used a sports utility vehicle (SUV) to transport and deploy the iHFUAM, and we chose a river embankment near the survey area to take off and land (Figure 3). The iHFUAM could be manually or autonomously controlled by an experienced pilot during take-off or landing. When flying over the survey lines, it followed predefined paths autonomously. We monitored the diurnal variations of the magnetic field during the survey flights.



Figure 6. Designed survey lines: (a) Satellite image of the survey area with overlaid elevation (elevation display ratio adjusted to 5 times for better visualization); (b) designed survey lines (green).

We completed the field survey in one day with two flights. The first sortie lasted 2.4 h and the second one lasted 3 h. During the flight, the aircraft control computer autonomously

flew according to the preset routes and altitudes, with an average flight speed of about 90 km/h to 100 km/h and a magnetic data sampling rate of 10 Hz. We acquired a total of 372 km of aeromagnetic data with an average line spacing of 250 ± 1.3 m and an average flight altitude (distance to the ground) of 152 m (Figure 7). Figure 7 shows that the iHFUAM had outstanding position control, even under the influence of the unexpected windy and chilly weather on the flight day. Most of the line deviations were less than 5 m, with only a few deviations of more than 10 m in the north corner. The actual measured height from the ground was generally between 140 and 160 m, which met our intended goal of an average flight altitude of 150 m. Please note that we increased the planned flight altitude from 100 m to 150 m for safety reasons in windy conditions after rainy and snowy weather. Additionally, the main objective of this measurement was experimental and for validation, which allowed us to make temporary adjustments to the flight altitude.

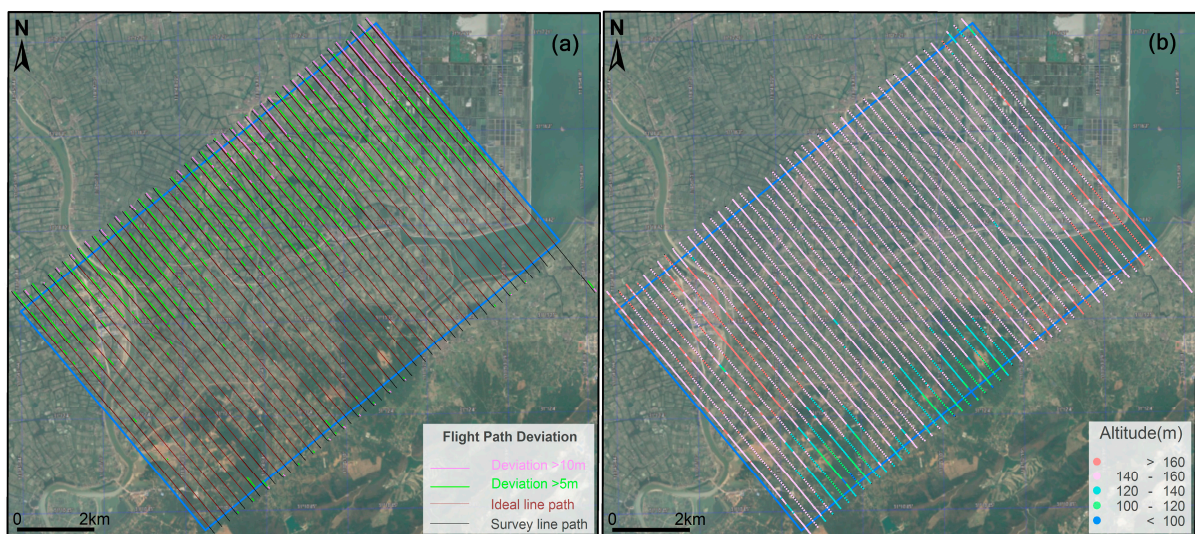


Figure 7. Position and altitude deviations of the field survey: (a) Flight path deviations; (b) color range symbols of altitudes.

We created simple illustrations of the total magnetic intensity (TMI) data using a straightforward approach, where we first calculated the average value of all TMI measurements and used this average as a baseline. TMI values greater than the average were assigned warm colors, while those less than the average were assigned cool colors. Based on this approach, we generated two graphical representations of the TMI data: a color zone scatter plot (Figure 8a) and a profile plot (Figure 8b) along the survey lines. Figure 8a allows for a quick observation of the planar distribution of TMI within the survey area, which consists of two high-value areas at the northeast and southwest ends, respectively, and a low-value area in the center. The difference between the maximum and minimum TMI values is approximately 500 nT. In comparison, Figure 8a,b shows similar magnetic field features but provides a more intuitive representation of TMI magnitude across the survey area based on distance. Figure 8b shows that the strongest magnetic field intensity is in the northeast, while the southwest has a relatively weaker magnetic field intensity. Both figures show a prominent TMI high-value area associated with the Chating deposit, which is likely related to the presence of concealed intrusive rocks, as discussed earlier. Furthermore, it is reasonable to speculate that other concealed intrusive rocks may exist beneath the high-value areas in the northeast and southwest based on these findings.

3.4. Corrections

During airborne magnetic surveys, errors can arise in measurement data due to changes in the Earth's magnetic field over time, differences in instrument installation

methods, and inherent magnetic interference from the system. As a result, it is essential to correct the raw data obtained from measurements to ensure higher quality data [27].

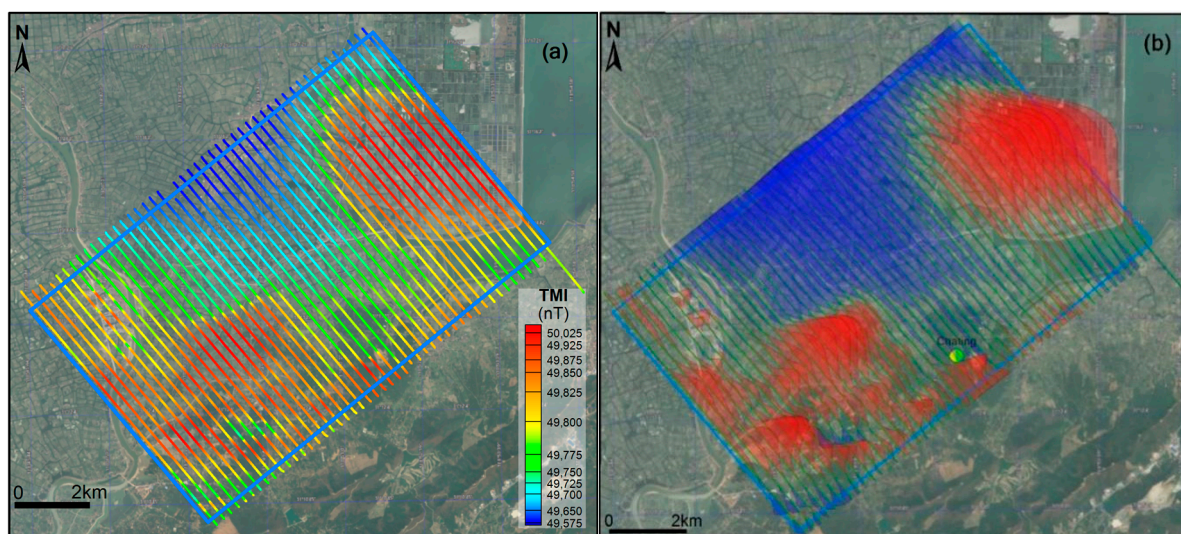


Figure 8. Color zone symbols plot and profile plot of TMI in survey area: (a) Color zone symbols; (b) profile map of TMI (The profile base is 49,800 nT. TMI values greater than 49,800 are filled in red, and the values less than it are filled in blue. On the direction perpendicular to the survey lines, 1 km represents a magnetic field strength of 250 nT.).

3.4.1. Diurnal Variation Correction (DVC)

During the flying time, the magnetic diurnal variation data was synchronously recorded using a magnetic base station, with a recording rate of 10 Hz. The measurement data of the base station was subtracted from the aeromagnetic data using the GNSS time channel as a reference to eliminate the effect of the diurnal variation of the geomagnetic field on the measurement data.

3.4.2. Lag Correction

The magnetometer of iHFUAM is installed 1.5 m away in front of the nose, while the GNSS antenna is installed above the cabin, resulting in a positional difference of approximately 2.5 m between them. Therefore, the recorded magnetic field values during flight are always relatively forward in position, causing a positional difference on different flight lines. Lag correction is the process of appropriately dragging the magnetic field values backward to achieve consistency between the magnetic field values and spatial positions. Considering the flight speed of about 90–100 km/h and the data sampling rate of 10 Hz, the estimated sampling point distance is approximately 3 m. Therefore, we performed one fiducial lag correction on the magnetic data after DVC.

3.4.3. Heading Correction

Heading correction is usually employed to reduce errors caused by the inherent magnetic field of the aircraft in different directions. Generally, reciprocal measurements on two cross-intersection lines are used to obtain the correction parameters during field surveys. Due to the inability to carry out a compensation flight, we estimated the difference of two adjacent reverse measurement lines in the stable magnetic field area for heading correction. Corrections of -3 nT and $+3$ nT for the northwest and southeast measurement lines were applied, respectively.

3.4.4. Removal of IGRF

To eliminate the influence of changes in the Earth's magnetic field with respect to geographical coordinates and altitude on the measurement data, we used the 13th generation

International Geomagnetic Reference Field (IGRF 13) to calculate the normal magnetic field value for each measurement data and corrected them point by point.

After applying these corrections, we obtained what is typically referred to as the magnetic anomaly (MA). In fact, due to the iHFUAM being based on small- to medium-sized UAVs with low inherent interference, only minor adjustments were made to the lag correction and heading correction, which achieved satisfactory results in this survey.

3.5. Noise Level of the Magnetic Data

As mentioned above, due to airspace restrictions and precipitation, we were unable to carry out measurement flights, such as tie lines and repeat lines. To evaluate the quality of the measurement data, we calculated the fourth difference noise of the magnetic field on the survey line, which can, to some extent, represent the data quality during dynamic measurement.

The fourth difference for the magnetic data can be calculated as follows:

$$\text{fourth difference} = \frac{T_{-2} - 4T_{-1} + 6T_0 - 4T_{+1} + 2T_{+2}}{16} \quad (1)$$

where T_{-2} , T_{-1} , T_{+1} , and T_{+2} are two consecutive readings before and after the current magnetic field T_0 , respectively.

As an example, we calculated the fourth difference of the survey line passing through the Chating deposit and plotted the profile together with the magnetic field values (Figure 9a). Additionally, we calculated the fourth difference of the aeromagnetic data for all survey lines and performed histogram statistics. The results showed that the majority of the fourth differences of the aeromagnetic data were between ± 0.01 nT (Figure 9b). This can be considered as a good level of aeromagnetic noise, from an industry-standard (between ± 0.05 nT) perspective [23,28].

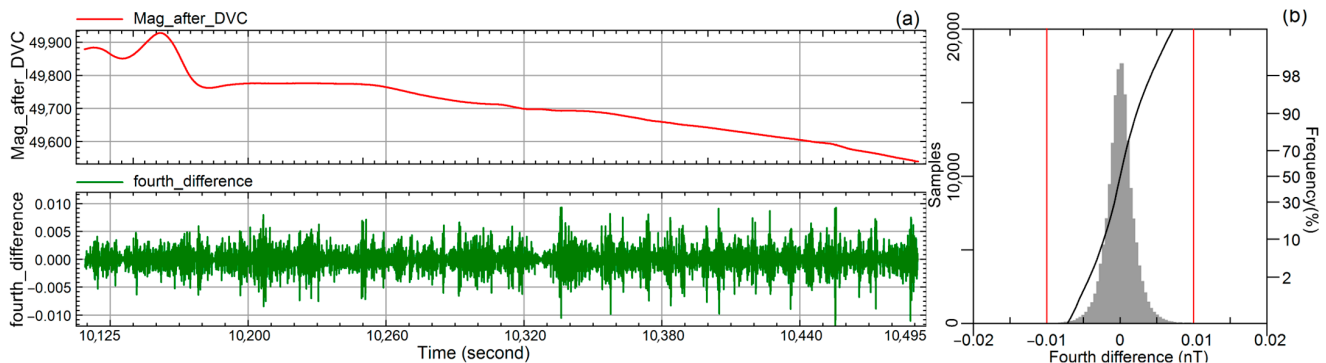


Figure 9. Profile of fourth differences and histogram statistics: (a) Curves of magnetic data after diurnal variation correction and its fourth difference of the survey line passing through Chating deposit; (b) histogram statistics map of fourth differences of all aeromagnetic data.

3.6. Gridding and Transformations

3.6.1. Gridding

The MA data are usually transformed into grid data after the corrections. Grid data is more regular and facilitates statistical analysis and visualization. Moreover, gridding reduces data volume, improves data processing efficiency, and facilitates further processing and analysis. Generally, the grid cell size is recommended to be between one-fourth and one-third of the line spacing [29]. In this case, the line spacing is 250 m, and the typical cell size should be around 75 m. However, since the flight altitude is slightly higher at around 150 m, we adjust the grid cell size to 100 m and use the minimum curvature method to grid MA (Figure 10a).

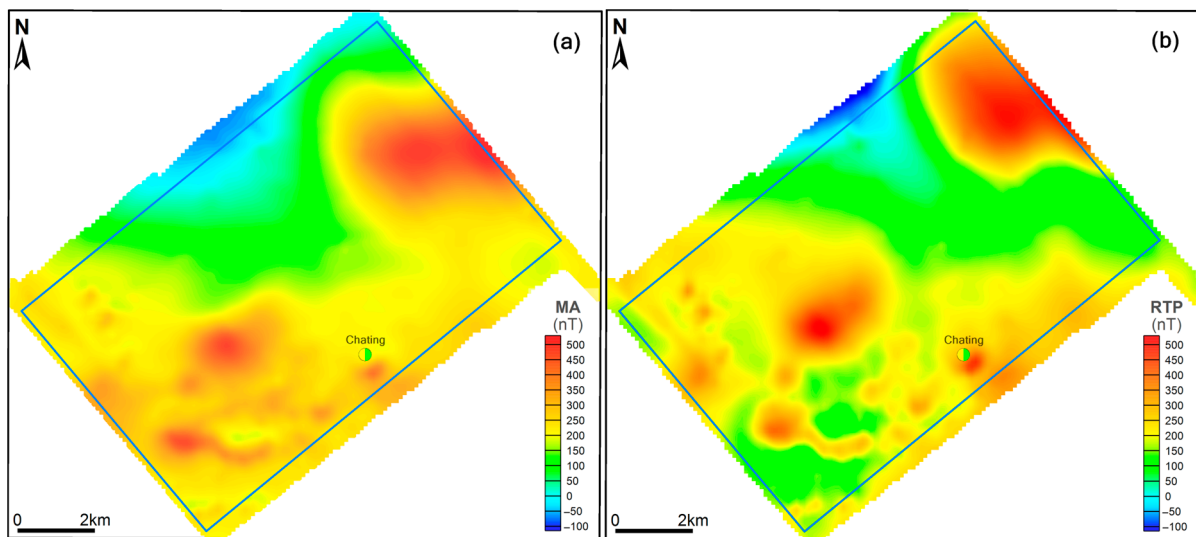


Figure 10. Color map of MA and RTP data: (a) MA; (b) RTP.

3.6.2. Reduce to Pole

Reduce to pole (RTP) is a useful method for magnetic data processing. RTP converts the magnetic data to a direction perpendicular to the Earth's surface. Essentially, it removes the dipolar nature of magnetic anomalies through computations, allowing the anomalies to better correspond to the geological source bodies. We applied the RTP transformation to the MA of the study area using a geomagnetic inclination of 47.67 degrees and a declination of -5.87 degrees. As a result of RTP, the range of most anomalies is reduced, and their morphology becomes simpler, making the data easier to interpret and utilize (Figure 10b).

From Figure 10, it is evident that after performing the RTP process, there were clear changes in the magnetic anomaly distribution in the surveyed area. The central positions of several major anomalies shifted northward. Moreover, the core ranges became more concentrated, reflecting more accurately the locations and sizes of magnetic geological features.

3.7. Interpretation

Three-dimensional (3D) inversion is currently an important data processing and interpretation technique in magnetic surveying. Compared to profile maps and contour maps, 3D inversion can obtain 3D magnetic structural information of underground space, which reflects the magnetic structure underground more intuitively. There are mainly two types of 3D inversion: shape model inversion and automatic property model inversion. The 3D automatic property model inversion divides the underground source area into regular hexahedral composite unit models, forming a 3D regular mesh of hexahedral units. During the inversion calculation, the shapes of these units remain unchanged while their properties change, and the distribution of magnetic sources is depicted by changes in properties to achieve the inversion purpose. Due to its advantages, such as an easy operation of model properties, an ability to simulate any complex geological body, and a few restrictions on method technology, 3D automatic property inversion has always been the mainstream research direction of three-dimensional inversion. However, it has faced two major challenges: the problem of multiple solutions and the problem of computation time. Scholars have addressed these two issues by imposing additional constraints to constrain the inversion process and by carrying out deep research and applying optimizing inversion algorithms and using multi-core parallel technology to improve computation speed [30–43].

We conducted a rapid self-constrained three-dimensional magnetization inversion of aeromagnetic data using MAG3D, which was developed by the Geophysical Inversion Research Team at the University of British Columbia based on the research by Li et al. [30–32]. And, it is currently one of the most widely used magnetic three-dimensional property inversion modules. Based on the existing basic geological information, we expected that the

magnetic geological bodies within the study area were not particularly complex. To quickly obtain three-dimensional magnetization information, we created a simple regular 3D mesh file with a cell side length of 200 m each, and with 83 cells in the eastward direction, 78 cells in the northward direction, 20 cells in the depth direction. With two strong magnetic anomalies on the boundary, four additional cells in each direction were added to reduce boundary effects. We used the default parameters of MAG3D to perform a self-constrained and fast three-dimensional magnetization inversion: The input data were the designed mesh file and measured aeromagnetic data (magnetic field values multiplied by 5% and plus 0.01 nT as uncertainty noises); the sensitivity file was automatically generated by the program, using the default depth weighting parameter $\beta = 3$; the inversion mode was the default discrepancy mode; the smoothing coefficient used the default parameters $\alpha_s = 0.0001$ and $\alpha_x = \alpha_y = \alpha_z = 1$; the initial SI was set to 0.0001, and the lower and upper bounds of SI were set to 0 and 1, respectively. Then, we obtained the magnetization spatial information within the 4 km depth range. Figure 11 illustrates the forward response of the inversion susceptibility model and the difference between observed data and forward data. It can be observed that the large errors are mainly distributed in the complex magnetic field area with a larger magnetic gradient in the southern part of the survey area.

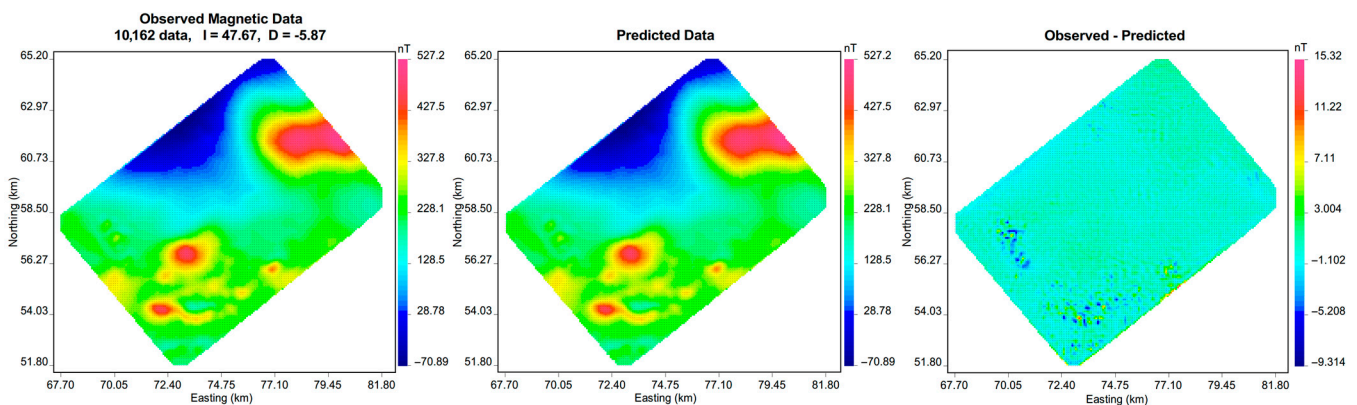


Figure 11. Forward response of the inversion result and the difference between it and the observed data.

Figure 12 shows the results of the inversion, including the 3D voxel model of the entire area, five vertical sections along the survey lines, one vertical section along the perpendicular line, and a geological section of the Chating deposit. According to the summarized magnetic characteristics of rocks (Table 1), it can be observed that the range of magnetization susceptibility of the intrusive rocks within the survey area is approximately several thousand times 10^{-6} SI. Then, we clipped the display range of cells by adjusting the susceptibility values in the 3D view and compared it with the geological section of the Chating deposit to make the displayed cells range roughly equivalent to the intrusive rock in the geological section. And, we found that setting the minimum susceptibility value to 5000×10^{-6} (i.e., 0.005) SI corresponds well with the range of remaining cells and the range of intrusive rocks in the geological section (Figure 13). Therefore, from the perspective of simple deduction, we consider that the cells with susceptibility greater than 0.005 SI represent the areas where intrusive rocks were present in the survey area.

As we do not have any other data besides the measured aeromagnetic data, the profile map of the Chating deposit, and the magnetic susceptibility data of samples, we believe that the mineralization background and conditions in the measurement area are highly similar. Since the measurement area is a small region of only a few square kilometers, we can use simple logical deductions, such as “from known to unknown” and “from near to far”, to preliminarily speculate the ore prospects in this area.

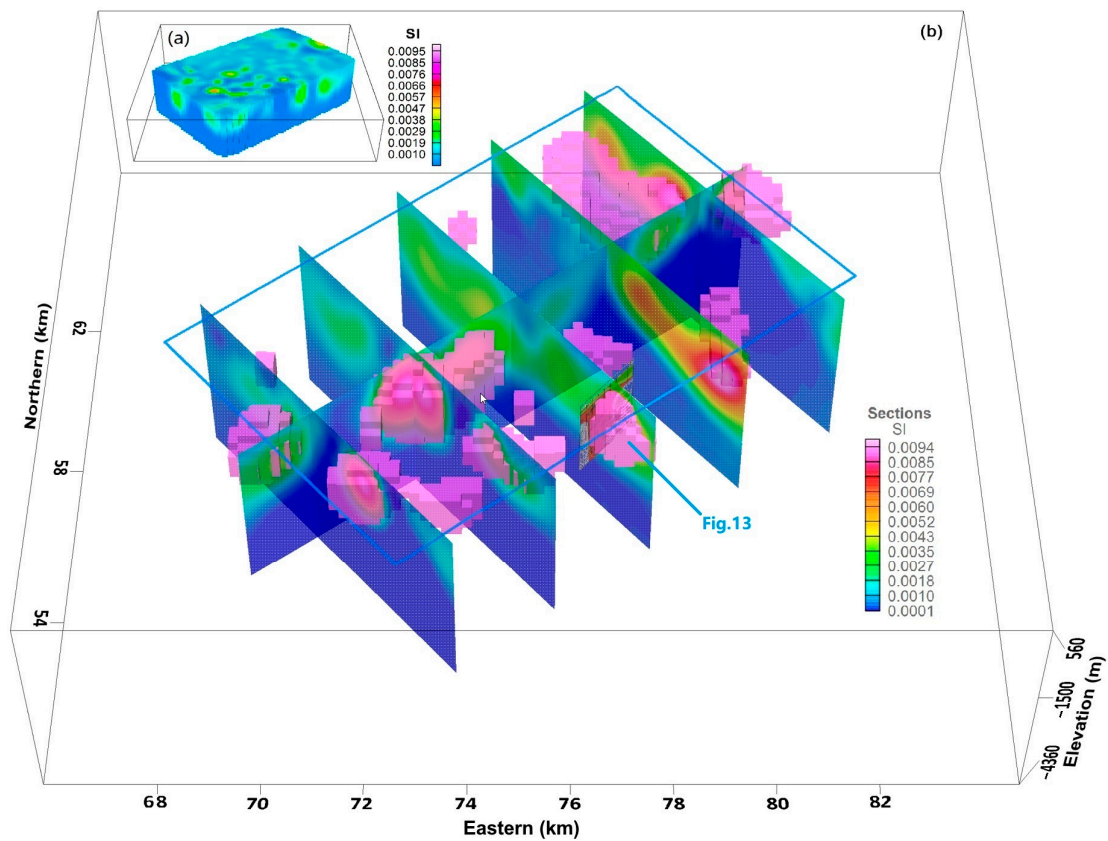


Figure 12. The inversion results of magnetic susceptibility and the inferred distribution of intrusive rocks in the survey area: (a) The 3D magnetic susceptibility inversion results; (b) slices of the magnetic susceptibility voxel data and cells with magnetic susceptibility greater than 0.005 SI.

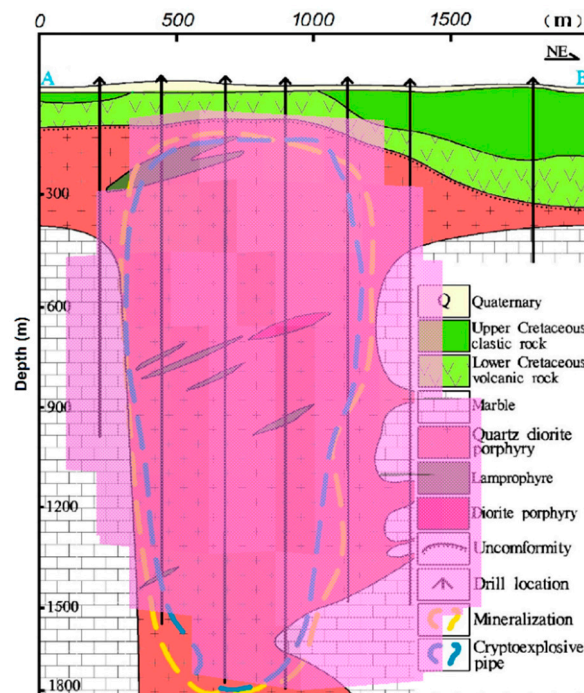


Figure 13. The comparison between the three-dimensional magnetic susceptibility inversion results on the Chating deposit and the geological section shows a good correspondence between the cells with magnetic susceptibility greater than 0.005 and the intrusive rocks.

The cells interpreted as intrusions are shown in a top view, and the range of the rock mass will be projected onto the surface. We can use this to circle the planar distribution range of the intrusive rock mass and number them from R1 to R12 (Figure 14). From Figure 14, we find the Chating deposit has a very good correlation with R1. We assume some simple principles for judging the possibility of mineralization in other rock masses:

1. Rock masses closer to R1 are more likely to be mineralized, mainly R2, R3, R4, R5, R6, R7, and R8.
2. Rock masses with similar shapes and sizes to R1 have more similar ore-forming conditions to R1, mainly R2, R3, R5, R8, R9, and R12.
3. Rock masses in the same local structural zone as R1 are more likely to be mineralized, mainly R2, R3, R4, R5, R6, R7, R8, R9, and R10.

By simply intersecting the rock mass classification sets defined by the three principles, we can group the rocks from high to low mineralization potential. In other words, we can recommend the priority order for subsequent exploration work:

1. R2, R3, R5, R8 (Red-dashed polygons in Figure 14).
2. R4, R6, R7, R9 (Blue-dashed polygons in Figure 14).
3. R10, R11, R12 (Green-dashed polygons in Figure 14).

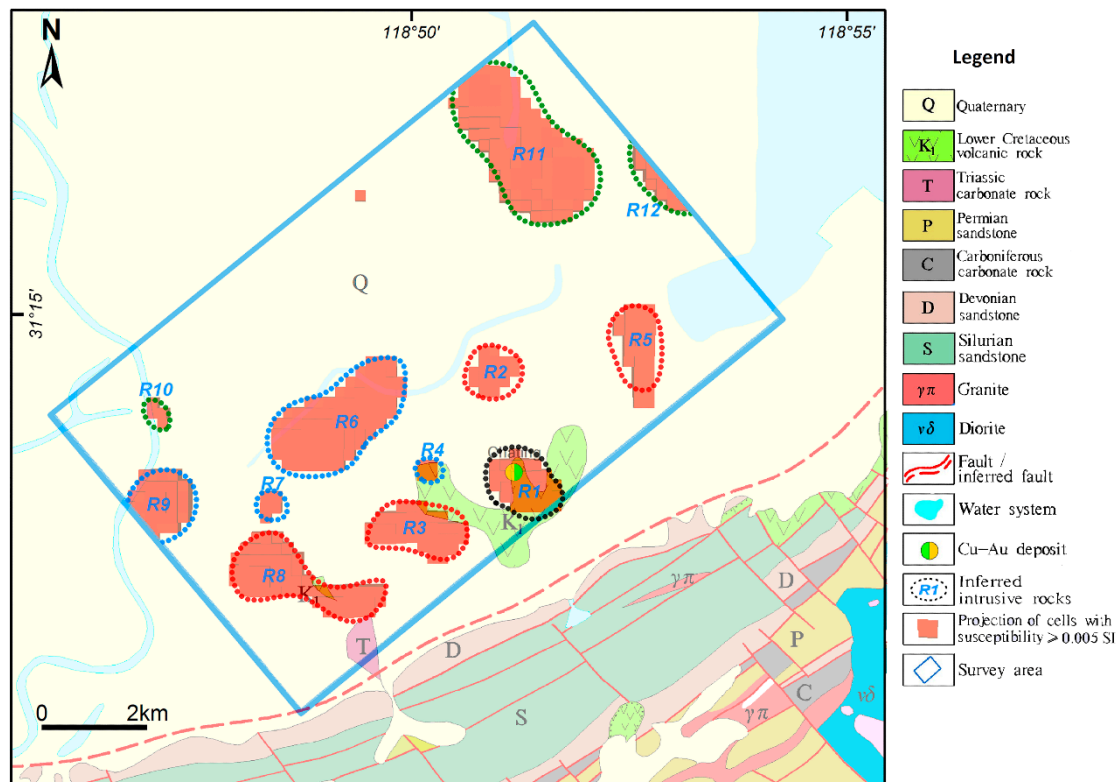


Figure 14. The projection of the cells with susceptibility greater than 0.005 SI in inversion results onto the geological map.

4. Discussion and Conclusions

To meet the practical needs of small space and light load for small- and medium-sized UAVs, we have developed the iMAMS, which is integrated into a hybrid fixed-wing UAV to form the iHVUAM. The iHVUAM experimental measurement and mineral exploration prediction applications have been carried out around the known Chating deposit. By means of a rapid 3D magnetic susceptibility inversion, 12 intrusive rock masses have been delineated, and the order of subsequent exploration work has been recommended. Other researchers have carried out explorations based on gravity, magnetism, controlled-source

audio-frequency magnetotellurics (CSAMT) and have also conducted drilling validation in this area. They have discovered lead–zinc–silver and lead–zinc–gold deposits in the R2 and R8 areas, respectively.

Based on the above work, we can draw several conclusions:

1. Compared to traditional aeromagnetic systems used on manned aircrafts, the iMAMS has a smaller size and weight. The host weight is approximately 2.5 kg, and the entire system weight with a OPM is about 6.5 kg. It is already quite suitable for use in medium- and small-sized UAV-borne aeromagnetic systems.
2. The iHFUAM is compact and very flexible to deploy. It only requires three people to conduct a flight survey. The ability of VTOL in the survey area as well as the flight speed of about 90 km/h to 100 km/h with a maximum endurance of 3.5 h in a single sortie are all helpful in improving the measurement efficiency. The ability to fly autonomously on a predefined path enables a very good flight control quality and lower magnetic interference from the UAV itself and is beneficial for acquiring good data. The iHFUAM already has the essential capabilities to provide efficient and flexible aeromagnetic measurements.
3. As the earliest developed and most widely used and mature measurement method in airborne geophysical exploration, magnetic surveying has the characteristics of being fast and efficient. In addition to directly searching for magnetic minerals, such as magnetite, it has been proven to be an effective mineral exploration method by indirectly delineating mineralized rock masses with magnetic properties by using technical means, such as 3D susceptibility inversion.
4. Although the iHVUAM has obtained satisfactory data for us at the time, we must acknowledge that the work process was not good enough due to various constraints. To achieve better development, integrating the compensation module is an important task that we will undertake in the follow-up work.

5. Patents

There is a patent authorized by China National Intellectual Property Administration resulting from this work (Authorization No. ZL202120873578.3).

Author Contributions: Conceptualization, N.L., J.L. and W.G.; methodology, N.L., W.G. and J.L.; software, J.L.; validation, J.L., Y.X. and H.Z.; formal analysis, N.L.; investigation, W.G., Y.L. (Yongbo Li), and N.L.; resources, J.L. and G.L.; data curation, N.L.; writing—original draft preparation, N.L. and J.L.; writing—review and editing, Y.L. (Yongbo Li) and N.L.; visualization, Y.L. (Yu Liu); supervision, G.L. and Z.C.; project administration, N.L.; funding acquisition, N.L. All authors have read and agreed to the published version of the manuscript.

Funding: This research was funded by the National Nonprofit Institute Research Grant of IGGE (Grant No. AS2022J01), China Geological Survey (Grant No. DD20230245 and No. DD20221639), National Key Research and Development Program of China (No. 2016YFC0600209).

Acknowledgments: The authors would like to thank the geophysical research team of JOUAV for their kind help and great work. And, we would like to express our sincere appreciation to the reviewers and editors for their professional and valuable suggestions.

Conflicts of Interest: The authors declare no conflict of interest.

References

1. Bona, K.; Seulki, L.; Gyesoon, P.; Seong-Jun, C. Development of an Unmanned Airship for Magnetic Exploration. *Explor. Geophys.* **2021**, *52*, 462–467. [[CrossRef](#)]
2. Baogang, Z.; Ziqi, G.; Yanchao, Q. A Simplified Aeromagnetic Compensation Model for Low Magnetism UAV Platform. In Proceedings of the 2011 IEEE International Geoscience and Remote Sensing Symposium, Vancouver, BC, Canada, 24–29 July 2011; pp. 3401–3404.
3. Cao, Z.; Chen, D.; Yu, F.; Wang, H.; Zeng, Z. EMI Suppression of UAV Power in Aeromagnetic Survey. *IEEE Electromagn. Compat. Mag.* **2013**, *2*, 45–53. [[CrossRef](#)]

4. Lei, J.; Ziqi, G.; Baogang, Z. Scalar Calibration of Aeromagnetic Data Using BPANN and LS Algorithms Based on Fixed-Wing UAV Platform. *IEEE Trans. Instrum. Meas.* **2015**, *64*, 1968–1976. [[CrossRef](#)]
5. Hansen, C.R.D. Magnetic Signature Characterization of a Fixed-Wing Vertical Take-off and Landing (VTOL) Unmanned Aerial Vehicle (UAV). Master's Thesis, University of Victoria, Victoria, BC, Canada, 2018.
6. Tuck, L.E.; Samson, C.; Laliberté, J.; Cunningham, M. Magnetic Interference Mapping of Four Types of Unmanned Aircraft Systems Intended for Aeromagnetic Surveying. *Geosci. Instrum. Methods Data Syst.* **2021**, *10*, 101–112. [[CrossRef](#)]
7. Qiao, Z.-K.; Yuan, P.; Wang, L.-F.; Zhang, Z.-H.; Huang, Y.-S.; Zhang, J.-J.; Li, L.-L.; Zhang, Z.-Y.; Wu, B.; Lin, Q. Research on Aeromagnetic Compensation of a Multi-Rotor UAV Based on Robust Principal Component Analysis. *J. Appl. Geophys.* **2022**, *206*, 104791. [[CrossRef](#)]
8. Papakonstantinou, A.; Topouzelis, K.; Pavlogeorgatos, G. Coastline Zones Identification and 3D Coastal Mapping Using UAV Spatial Data. *ISPRS Int. J. Geo-Inf.* **2016**, *5*, 75. [[CrossRef](#)]
9. Alireza, M.; Lars, D.; Kent, P.; Alex, P.; Henrik, J.; Mehrdad, B.; Mats, W.; Paul, M. The Potential of Rotary-Wing UAV-Based Magnetic Surveys for Mineral Exploration: A Case Study from Central Sweden. *Lead. Edge* **2017**, *36*, 552–557. [[CrossRef](#)]
10. Parshin, A.; Grebenkin, N.; Morozov, V.; Shikalenko, F. First Results of a Low-Altitude Unmanned Aircraft System Gamma Survey by Comparison with the Terrestrial and Aerial Gamma Survey Data. *Geophys. Prospect.* **2018**, *66*, 1433–1438. [[CrossRef](#)]
11. Han, L.; Jian, G.; Haobin, D.; Xiangyu, Q.; Wang, L.; Huan, L.; Zhiwen, Y.; Jun, Z.; Haiyang, Z. Aeromagnetic Compensation of Rotor UAV Based on Least Squares. In Proceedings of the 2018 37th Chinese Control Conference (CCC), Wuhan, China, 25–27 July 2018; pp. 10248–10253.
12. Callum, W.; Alexander, B.; Georgia, F. Spectral Analysis of Magnetometer Swing in High-Resolution UAV-Borne Aeromagnetic Surveys. In Proceedings of the 2019 IEEE Systems and Technologies for Remote Sensing Applications Through Unmanned Aerial Systems (STRATUS), Rochester, NY, USA, 25–27 February 2019; pp. 1–4.
13. Calou, P.; Munschy, M. Airborne Magnetic Surveying with a Drone and Determination of the Total Magnetization of a Dipole. *IEEE Trans. Magn.* **2020**, *56*, 6000409. [[CrossRef](#)]
14. Mu, Y.; Zhang, X.; Xie, W.; Zheng, Y. Automatic Detection of Near-Surface Targets for Unmanned Aerial Vehicle (UAV) Magnetic Survey. *Remote Sens.* **2020**, *12*, 452. [[CrossRef](#)]
15. Zhipeng, Q.; Xiu, L.; He, L.; Wentao, L. First Results from Drone-Based Transient Electromagnetic Survey to Map and Detect Unexploded Ordnance. *IEEE Geosci. Remote Sens. Lett.* **2020**, *17*, 2055–2059. [[CrossRef](#)]
16. Porras, D.; Carrasco, J.; Carrasco, P.; Alfageme, S.; Gonzalez-Aguilera, D.; Lopez Guijarro, R. Drone Magnetometry in Mining Research. An Application in the Study of Triassic Cu–Co–Ni Mineralizations in the Estancias Mountain Range, Almeria (Spain). *Drones* **2021**, *5*, 151. [[CrossRef](#)]
17. Zheng, Y.; Li, S.; Xing, K.; Zhang, X. Processing and Interpretation of UAV Magnetic Data: A Workflow Based on Improved Variational Mode Decomposition and Levenberg–Marquardt Algorithm. *Drones* **2022**, *6*, 11. [[CrossRef](#)]
18. Zheng, Y.; Li, S.; Xing, K.; Zhang, X. Unmanned Aerial Vehicles for Magnetic Surveys: A Review on Platform Selection and Interference Suppression. *Drones* **2021**, *5*, 93. [[CrossRef](#)]
19. Li, W.J.; Qin, X.W.; Gan, X.P. The IGGE UAV Aero Magnetic and Radiometric Survey System. In Proceedings of the Near Surface Geoscience 2014—20th European Meeting of Environmental and Engineering Geophysics, Athens, Greece, 8 September 2014.
20. Lu, N.; Xi, Y.; Zheng, H.; Ben, F.; Liu, J. An Airborne Geophysical Survey System Based on CH3-UAV Platform(IUAGSS) and Its Applications. In Proceedings of the 81st EAGE Conference and Exhibition 2019, London, UK, 3 June 2019; Volume 2019, pp. 1–5.
21. Wu, J.; Zhi, Q.; Deng, X.; Wang, X.; Yang, Y. Joint Inversion with Borehole and Semi-Airborne TEM Data Based on Equivalent Filament Approximation. *Minerals* **2022**, *12*, 803. [[CrossRef](#)]
22. Xi, Y.-Z.; Liao, G.-X.; Lu, N.; Li, Y.-B.; Wu, S. Study on the Aeromagnetic System between Fixed-Wing UAV and Unmanned Helicopter. *Minerals* **2023**, *13*, 700. [[CrossRef](#)]
23. Jirigalatu, Krishna, V.; Silva, E.L.S.d.; Døssing, A. Experiments on Magnetic Interference for a Portable Airborne Magnetometry System Using a Hybrid Unmanned Aerial Vehicle (UAV). *Geosci. Instrum. Methods Data Syst.* **2021**, *10*, 25–34. [[CrossRef](#)]
24. Qingtian, L.; Guixiang, M.; Kun, Z.; Zhendong, L.; Jiayong, Y.; Danian, S.; Jianguang, H.; Xuejing, G. The Lithospheric Architecture of the Lower Yangtze Metallogenic Belt, East China: Insights into an Extensive Fe–Cu Mineral System. *Ore Geol. Rev.* **2021**, *132*, 103989. [[CrossRef](#)]
25. Lu, S.; Lan, X.; Zhao, L.; Zhang, Z.; Yang, X.; Zhao, Z.; Guo, D.; Xu, X.; Wang, Y.; Li, J.; et al. A 3D Investigation of Geological Structure and Its Relationship to Mineralization in the Nanling-Xuancheng Ore District, Middle-Lower Yangtze River Metallogenic Belt, China. *J. Earth Sci.* **2022**, *33*, 664–680. [[CrossRef](#)]
26. Xu, X.-Y.; Xu, X.-C.; Xie, Q.; Fu, Z.; Lu, S.; Zhao, L. Geological Features and Ore-Forming Mechanisms of the Chating Cu–Au Deposit: A Rare Case of Porphyry Deposit in the Middle–Lower Yangtze River Metallogenic Belt. *Ore Geol. Rev.* **2022**, *144*, 104860. [[CrossRef](#)]
27. Reeves, C. *Aeromagnetic Surveys: Principles, Practice and Interpretation*; Geosoft Inc.: Toronto, ON, Canada, 2005; pp. 5.3–5.10.
28. Cunningham, M.; Samson, C.; Laliberté, J.; Goldie, M.; Wood, A.; Birkett, D. Inversion of Magnetic Data Acquired with a Rotary-Wing Unmanned Aircraft System for Gold Exploration. *Pure Appl. Geophys.* **2021**, *178*, 501–516. [[CrossRef](#)]
29. Isles, D.J.; Rankin, L.R. *Geological Interpretation of Aeromagnetic Data*; Society of Exploration Geophysicists and Australian Society of Exploration: St Leonards, Australia, 2013; ISBN 978-0-643-09809-1.
30. Li, Y.; Oldenburg, D.W. 3-D Inversion of Magnetic Data. *Geophysics* **1996**, *61*, 394–408. [[CrossRef](#)]

31. Portniaguine, O.; Zhdanov, M.S. 3-D Magnetic Inversion with Data Compression and Image Focusing. *Geophysics* **2002**, *67*, 1532–1541. [[CrossRef](#)]
32. Li, Y.; Oldenburg, D.W. Fast Inversion of Large-Scale Magnetic Data Using Wavelet Transforms and a Logarithmic Barrier Method. *Geophys. J. Int.* **2003**, *152*, 251–265. [[CrossRef](#)]
33. Liu, S.; Fedi, M.; Hu, X.; Ou, Y.; Baniamerian, J.; Zuo, B.; Liu, Y.; Zhu, R. Three-Dimensional Inversion of Magnetic Data in the Simultaneous Presence of Significant Remanent Magnetization and Self-Demagnetization: Example from Daye Iron-Ore Deposit, Hubei Province, China. *Geophys. J. Int.* **2018**, *215*, 614–634. [[CrossRef](#)]
34. Williams, N.C. *Geologically-Constrained UBC–GIF Gravity and Magnetic Inversions with Examples from the Agnew-Wiluna Greenstone Belt, Western Australia*; University of British Columbia: Vancouver, BC, Canada, 2008. [[CrossRef](#)]
35. Harrouchi, L.; Hamoudi, M.; Bendaoud, A.; Beguiret, L. Application of 3D Euler Deconvolution and Improved Tilt Angle to the Aeromagnetic Data of In Ouzzal Terrane, Western Hoggar, Algeria. *Arab. J. Geosci.* **2016**, *9*, 508. [[CrossRef](#)]
36. Reza, G.; Hosseinali, G.; Moslem, F. Regularized Nonlinear Inversion of Magnetic Anomalies of Simple Geometric Models Using Occam’s Method: An Application to the Morvarid Iron-Apatite Deposit in Iran. *Acta Geod. Geophys.* **2017**, *52*, 555–580. [[CrossRef](#)]
37. Marcelo, L.-S.; Yaoguo, L.; Roberto, M. Application of 3D Magnetic Amplitude Inversion to Iron Oxide-Copper-Gold Deposits at Low Magnetic Latitudes: A Case Study from Carajas Mineral Province, Brazil. *Geophysics* **2015**, *80*, B13–B22. [[CrossRef](#)]
38. Shuang, L.; Xiangyun, H.; Jianchao, C.; Jianhui, L.; Chunling, S.; Wei, W.; Qi, H.; Yajun, L. Inversion of Borehole Magnetic Data for Prospecting Deep-Buried Minerals in Areas with near-Surface Magnetic Distortions: A Case Study from the Daye Iron-Ore Deposit in Hubei, Central China. *Near Surf. Geophys.* **2017**, *15*, 298–310. [[CrossRef](#)]
39. Tavares, M.A.; Jiajia, S.; Yaoguo, L. Geophysical Inversions Applied to 3D Geology Characterization of an Iron Oxide Copper-Gold Deposit in Brazil. *Geophysics* **2017**, *82*, K1–K13. [[CrossRef](#)]
40. Shuang, L.; Xiangyun, H.; Rixiang, Z. Joint Inversion of Surface and Borehole Magnetic Data to Prospect Concealed Orebodies: A Case Study from the Mengku Iron Deposit, Northwestern China. *J. Appl. Geophys.* **2018**, *154*, 150–158. [[CrossRef](#)]
41. Shida, S.; Chao, C.; Yiming, L. Constrained 3D Inversion of Magnetic Data with Structural Orientation and Borehole Lithology: A Case Study in the Macheng Iron Deposit, Hebei, China. *Geophysics* **2019**, *84*, B121–B133. [[CrossRef](#)]
42. Meng, F.; Li, X.; Chen, Y.; Ye, R.; Yuan, F. Three-Dimensional Mineral Prospectivity Modeling for Delineation of Deep-Seated Skarn-Type Mineralization in Xuancheng–Magushan Area, China. *Minerals* **2022**, *12*, 1174. [[CrossRef](#)]
43. Li, H.; Li, X.; Yuan, F.; Jowitt, S.M.; Dou, F.; Zhang, M.; Li, X.; Li, Y.; Lan, X.; Lu, S.; et al. Knowledge-Driven Based Three-Dimensional Prospectivity Modeling of Fe–Cu Skarn Deposits; a Case Study of the Fanchang Volcanic Basin, Anhui Province, Eastern China. *Ore Geol. Rev.* **2022**, *149*, 105065. [[CrossRef](#)]

Disclaimer/Publisher’s Note: The statements, opinions and data contained in all publications are solely those of the individual author(s) and contributor(s) and not of MDPI and/or the editor(s). MDPI and/or the editor(s) disclaim responsibility for any injury to people or property resulting from any ideas, methods, instructions or products referred to in the content.